Materials Science and Engineering A 527 (2010) 3186–3194

Contents lists available at ScienceDirect

Materials Science and Engineering A

journal homepage: www.elsevier.com/locate/msea

Kinetics modeling of austenite decomposition for an end-quenched 1045 steel

Seok-Jae Lee, Erik J. Pavlina*, Chester J. Van Tyne

Advanced Steel Processing and Products Research Center, Department of Metallurgical and Materials Engineering, Colorado School of Mines, Golden, CO 80401, USA

ARTICLE INFO

Article history:
Received 7 December 2009
Received in revised form 21 January 2010
Accepted 26 January 2010

Keywords:
Transformation kinetics
Austenite decomposition
End-quenching test
1045 steel
Finite element simulation

ABSTRACT

Finite element simulations that predict the microstructure and properties of heat-treated steels can be significantly improved by incorporating appropriate models for the kinetics of various austenite transformations. In the present study the austenite decomposition kinetics for a 1045 steel was modeled using a modification of the transformation equation proposed by Li et al. [1]. The kinetics of the continuous cooling transformation were determined directly from an isothermal transformation diagram. To verify the predictions of the model, an end-quench test was used because it produces a wide range of microstructures. The microstructures predicted by the kinetics model for the end-quenched sample were confirmed by quantification of the microstructures observed in the end-quench experiments. Furthermore, the predicted hardness profile was in good agreement with the experimentally measured hardness profile. The kinetics model developed in the present study was compared to the models proposed by Kirkaldy and Venugopalan [2] and the unmodified model by Li. The present model provides a more accurate prediction. A microstructural-based hardness equation from the literature was also evaluated and it predicted hardness values that were above the experimentally measured values. The model we propose predicts the experimental hardness profile more accurately, since it is based on the calculated microstructure and experimental hardness values of martensite, bainite, and ferrite/pearlite.

1. Introduction

Microstructural changes during austenite decomposition depend on the transformation temperature region and cooling rate. Over the years, many experimental studies have been performed to reveal the microstructural changes during isothermal holding or continuous cooling of austenite for various kinds of steels. The isothermal transformation (IT) diagram, which is also called the time–temperature-transformation (TTT) diagram, and the continuous cooling transformation (CCT) diagram have been developed to graphically characterize the decomposition transformation as a function of time and temperature.

However, when these diagrams are based on experimental measurements, several limitations are present. Each diagram is limited because the temperatures at which specific transformations occur can vary due to several factors, such as: (1) the chemical composition of steel, (2) the solid solution condition in the austenite prior to cooling and transformation, (3) the presence of precipitates in austenite, (4) the prior austenite grain size, and (5) the applied stresses during the transformation. For applicability over a wide range of conditions, any generalized equation or model that is used to predict the transformation diagram should include these limiting factors.

There are two methods to develop a model for transformation kinetics of metals. The first method is to create a model based on thermodynamic calculations; the second method is to empirically determine a model based on experimental data. The former is the "ideal" method, since it is not dependent on experiments and only depends on theoretical parameters obtained from basic material properties. The model derived by thermodynamic and kinetic calculations has greater physical meaning than a model derived by empirical methods. However, it is not easy to obtain all of the basic parameters required for commercial materials whose chemical compositions can vary, due to the wide range of alloys used in the various grades and even within a single grade. Thus, many researchers have developed empirical kinetics models based on experimental data to study and characterize solid-state transformations [1–16].

A general equation to model isothermal transformation kinetics was proposed by Johnson and Mehl [3], Avrami [4], and Kolmorgorov [5] (JMAK) to calculate the product phase volume fraction as a function of time under isothermal conditions, and has been used for general transformation in steels [17]. However, in most cases austenite decomposition is non-isothermal and the principle of additivity proposed by Scheil [6] and further developed by Avrami [7] can enable the JMAK kinetics equation to be used under non-isothermal conditions.

* Corresponding author. Tel.: +1 303 273 3106; fax: +1 303 273 3016.
E-mail address: epavlina@mines.edu (E.J. Pavlina).

0921-5093/$ – see front matter © 2010 Elsevier B.V. All rights reserved.
doi:10.1016/j.msea.2010.01.081

Table 1
Values for empirical constants in density equation $\rho = a_\rho + b_\rho \cdot T + c_\rho \cdot T^2$.

Structure	a_ρ (kg/m^3)	b_ρ (kg/m^3-K)	c_ρ (kg/m^3-K^2)	Standard error for a_ρ	Standard error for b_ρ	Standard error for c_ρ
Austenite (above 1041 K)	8190	−0.49		10.6	0.0111	
Ferrite + carbide (below 985 K)	7919.7	−0.2149	-102.0×10^{-6}	0.078	0.00026	0.21×10^{-6}

Regression of data every 10 K from Thermo-Calc using the TCFE3 database [24].

Cahn [18] proved that the non-isothermal transformation can be calculated from an isothermal equation, like the JMAK equation, by using the additivity rule. Lusk and Jou [19] suggested that restricted conditions exist for the application of the additivity rule for phase transformation kinetics. They argue that the additivity rule is applicable for any general isokinetic relationship. An expression of a general isokinetic relationship – where the volume fraction dependence and the temperature dependence are separable – can be derived from the JMAK equation, to give

$$\frac{dV}{dt} = K(T)^{1/n} \cdot n \cdot (1-V) \cdot \left(\ln\frac{1}{1-V}\right)^{(n-1)/n} = f(T) \cdot g(V) \quad (1)$$

where V is the volume fraction of the product phase, T is temperature, and t is time. The parameters K and n are the constants related to the transformation rate obtained from the experimental data. Since $f(T)$ is a function of temperature and $g(V)$ is a separable function of volume fraction, the additivity rule is valid for Eq. (1). Other similar studies have addressed the limitations of the additivity rule [20–22].

Over the last two decades, many studies have been performed to quantitatively characterize the austenite decomposition phenomenon using phase-transformation kinetics. Several studies have focused on the diffusional transformation kinetics occurring during cooling in low alloy steels. Kirkaldy and Venugopalan [2] have suggested kinetic models for diffusional transformations (i.e. the transformation of austenite to ferrite, pearlite, or bainite) based on published IT diagrams. They considered the effects of wide-ranging chemical composition, austenite grain size, and undercooling below the equilibrium transformation temperature. Lee and Bhadeshia [14] used nucleation theory and fitted constants to suggest the predictive model for the IT diagram. Li et al. [1] modified the kinetics models proposed by Kirkaldy and Venugopalan [2] by using published CCT diagrams. Their transformation kinetic models have been used to predict microstructural changes and mechanical properties of final products in real manufacturing processes by coupling the kinetics models with heat-transfer and thermal-stress analyses. The accuracy of a transformation kinetics model is the key factor for an accurate thermomechanical analysis.

One method to verify the accuracy of transformation kinetics model is a Jominy end-quench hardenability test, because of the wide range of cooling rates that are captured in a single experiment [23].

The objective of the present investigation was to examine several microstructural kinetics models for a 1045 plain carbon steel. In order to assess kinetics modeling of austenite decomposition, an end-quench hardenability test simulation was created. Evaluation of each model was made to determine how well the model predicted both the microstructure and the hardness profile of the end-quench test.

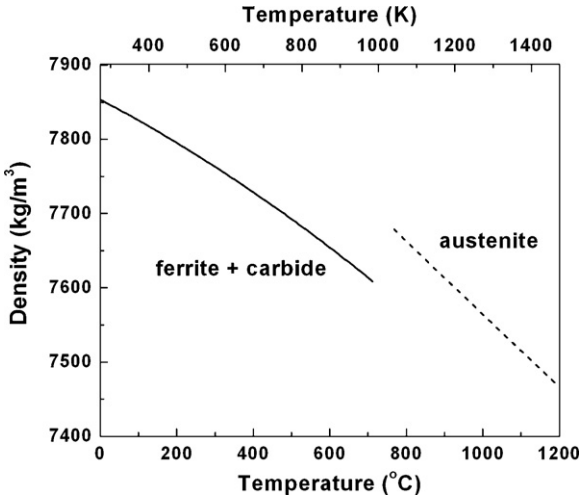

Fig. 1. Density variation with temperature for 1045 steel. Calculated with Thermo-Calc.

2. Material properties

For the modeling of the austenite decomposition of a 1045 steel, various physical properties are needed as a function of temperature. In the present study the thermal variation of density and specific heat as well as the latent heat of transformation were obtained by Thermo-Calc using the TCFE3 database [24]. Over the temperature range of interest Thermo-Calc was used to calculate the density and specific heat every 10 K. In order to use these data in a model the values were regressed by a linear or quadratic function of temperature.

The regression equation for the density, ρ (in kg/m^3) as a function of temperature, T (in K) is:

$$\rho = a_\rho + b_\rho \cdot T + c_\rho \cdot T^2 \quad (2)$$

where a_ρ, b_ρ and c_ρ are empirical constants. Table 1 lists the values of these constants for austenite and ferrite + carbide, as well as the standard error for each of the constants in the regression. Fig. 1 shows the density variation with temperature.

The regression equation for specific heat values, C_p, (in J/kg-K) as a function of temperature is:

$$C_p = a_C + b_C \cdot T + c_C \cdot T^2 \quad (3)$$

where a_C, b_C and c_C are empirical constants. Table 2 lists the values of these constants for austenite, ferrite, and ferrite + carbide as well as the standard error for the constants in the regression. Fig. 2 shows the specific heat variation with temperature. Each specific heat curve in Fig. 2 was calculated using data from Thermo-Calc

Table 2
Values for empirical constants in specific heat equation $C_p = a_C + b_C \cdot T + c_C \cdot T^2$.

Structure	a_C (J/kg-K)	b_C (J/kg-K^2)	c_C (J/kg-K^3)	Standard error for a_C	Standard error for b_C	Standard error for c_C
Austenite (above 1043 K)	439.0	0.1142		0.087	0.000068	
Ferrite (below 873 K)	435.	0.102	541×10^{-6}	7.3	0.027	23×10^{-6}
Ferrite + carbide (below 873 K)	447.	0.081	495×10^{-6}	6.0	0.022	19×10^{-6}

Regression of data every 10 K from Thermo-Calc using the TCFE3 database [24].

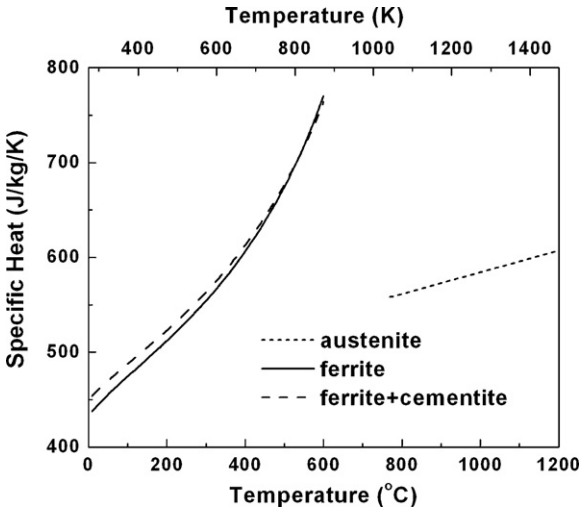

Fig. 2. Variation of specific heat with temperature for 1045 steel. Data were calculated with Thermo-Calc using the TCFE5 database.

based on the equilibrium volume fractions of phases in their stable temperature regions. The specific heat of the mixed ferrite and cementite phase was used for the pearlite and bainite microconstituents. The specific heats shown in Fig. 2 were extrapolated to encompass a larger temperature range than shown.

The temperature variation of the thermal conductivity, k, for the steel was obtained from the literature [25]. Fig. 3 shows the values of thermal conductivity as a function of temperature for a 1045 steel.

The latent heats for transformation of austenite to various phases were determined by Thermo-Calc to be as follows: (1) austenite to ferrite: 89.4 J/g; (2) austenite to pearlite: 77.5 J/g; and (3) austenite to bainite: 66.5 J/g. The latent heat for the transformation of austenite to martensite was obtained from the literature [26] and the value used was 81.5 J/g.

3. Transformation kinetics of 1045 steel

3.1. Transformation start temperatures

The equilibrium transformation start temperatures during cooling were calculated using published equations [27–30]. These equations account for the specific chemical composition of the steel. The ferrite transformation can begin below the A_{e3} temperature. The pearlite transformation occurs below the A_{e1} temperature when a volume fraction of pro-eutectoid ferrite reaches an equilibrium volume fraction. The bainite and martensite transformations occur below the bainite start (B_s) and martensite start (M_s) temperatures, respectively. Table 3 gives the calculated transformation temperatures for a 1045 steel.

Table 3
Calculated transformation temperatures (°C) for 1045 steel.

A_{e3}	A_{e1}	B_s	M_s
766	719	651	324

3.2. Equilibrium volume fraction of ferrite

Above the A_{e1} temperature, the transformed volume fraction of pro-eutectoid ferrite at a temperature is limited by an equilibrium phase boundary of austenite and austenite/ferrite, whereas the amount of pro-eutectoid ferrite below the A_{e1} temperature is determined by an extended line of equilibrium phase boundary of austenite and austenite/cementite, referred to as the A_{cm} temperature curve [31]. Fig. 4 shows the equilibrium volume fraction of pro-eutectoid ferrite for 1045 steel as a function of temperature. The maximum volume fraction is about 0.40 at the A_{e1} temperature.

3.3. Diffusional transformations

Kirkaldy and Venugopalan [2] proposed the kinetics model of diffusional transformation for low alloy steels based on published IT diagrams. Li et al. [1] modified Kirkaldy's kinetics model by using published CCT diagrams. The kinetics models of Li have been suggested for use in modeling various low alloy steels over a wide range of chemical compositions. In the current study the specified kinetics model for a 1045 steel was derived based on the published IT diagram [32] in conjunction with a slightly modified form of Li's kinetics models. The equation, which represents the diffusional transformation reactions, is based on the form of Eq. (1). The temperature factor is the same as Li et al. [1]. The factor involving the volume fraction of the specific constituent is similar to Li, but a linear variation term has been incorporated. The resulting equations

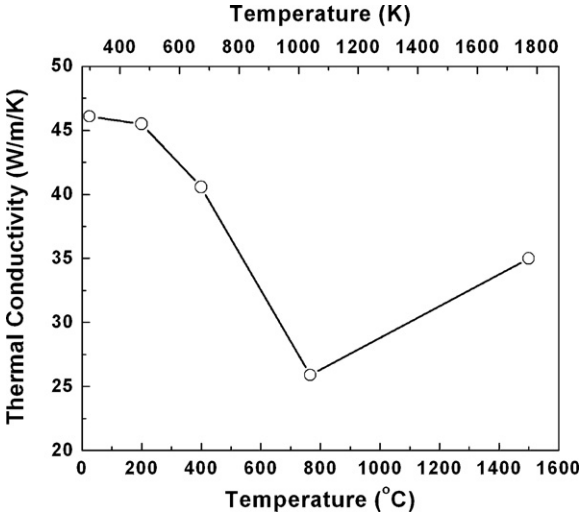

Fig. 3. Thermal conductivity variation as a function of temperature for 1045 steel [25].

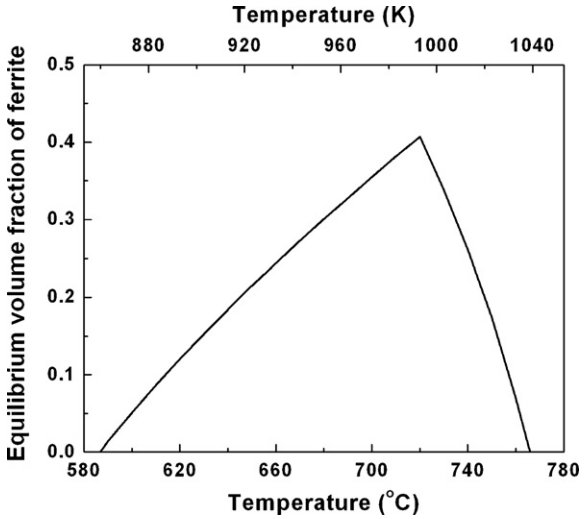

Fig. 4. Equilibrium volume fraction of ferrite both above and below the A_{e1} temperature.

Table 4
Values for parameters in the transformation rate equation.

Structure	A (1/s-K^n)	n	Q (kJ/mol)	T_{Trans} (°C)	a	b
Ferrite	0.213	3	115.546	766	0.75	1.2
Pearlite	2.38	3	115.546	719	1.41	0.37
Bainite	213.	2	115.546	651	0.44	0.32

n and Q obtained from the model by Li et al. [1]
A, a, and b obtained by simultaneous optimization of the three differential transformation equations.

are:

$$\frac{dV}{dt} = f(T) \cdot g(V) \tag{4}$$

with

$$f(T) = A \cdot (T_{Trans} - T)^n \cdot \exp\left(-\frac{Q}{RT}\right) \tag{5}$$

and

$$g(V) = \frac{V^{0.4\cdot(1-V)} \cdot (1-V)^{0.4\cdot V}}{a - b \cdot V} \tag{6}$$

where A, a, b, and n are an empirical constants, Q is an activation energy, T_{Trans} is the transformation temperature, T is absolute temperature, R is the gas constant (8.314 J/mol/K), and V is the volume fraction of the product microconstituent. Note that this kinetic equation for the decomposition of austenite in a 1045 steel have the form of Eq. (1). Hence, the additivity rule can be applied to each of the three diffusional transformations in this system.

The constants for these equations were determined from a nonlinear optimization of the experimental IT diagram. Table 4 lists the values used for the three transformation products resulting from a diffusion-controlled reaction – ferrite, pearlite, and bainite. The values of n and Q were obtained from Li's kinetics model [1]. The values of A, a, and b for three diffusional transformations were calculated simultaneously by using an optimization routine to compare the calculated results with total of 34 data points of a published 1045 IT diagram. The objective function, which was minimized when these optimized values were determined, is:

$$obj = \frac{1}{N}\sqrt{\sum_{i=1}^{N}\left(\frac{t_{\exp} - t_{cal}}{t_{\exp}}\right)^2} \tag{7}$$

where t_{exp} is the transformation time of experimental data point at a temperature, t_{cal} is the transformation time calculated at the same temperature, and N is the number of data points. If the model perfectly matched the data points then the value of the objective function would be 0.0. For the model of the three diffusion-controlled reactions, the final value of the minimized objective function was 0.097.

Fig. 5 shows the curves of a calculated IT diagram for 1045 steel using Eq. (4) for each product structure. The data points in Fig. 5 indicate the experimentally determined values for the starting and finishing transformations during isothermal heat treatments [32].

3.4. Martensitic transformation

Lee and Lee [33] have recently proposed a model for the martensitic transformation kinetics in plain carbon and low alloy steels. Their model is a function of both chemical composition and temperature. Their equation for the martensite transformation, which is used in the present study, is:

$$\frac{dV_M}{dT} = 0.0428 \cdot (M_s - T)^{0.191} \cdot V_M^{0.382} \cdot (1 - V_M)^{2.421} \tag{8}$$

where V_M is the volume fraction of martensite.

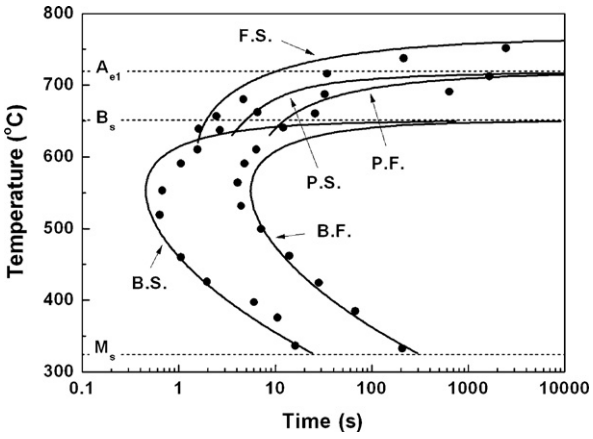

Fig. 5. Calculated isothermal transformation diagram using the kinetics model equation for 1045 steel. Data points are for the start and finish temperatures determined experimentally.

4. Finite element simulation

The transformation equations (Eqs. (4)–(6), and (8)), along with the material properties, were incorporated into a finite element analysis (FEA) simulation for the end-quench test. The commercial FEA software ABAQUS [34] was used for the simulations. ABAQUS was chosen because of its ability to allow the user to input specific material properties into the simulation. This ability was necessary so that the material properties and the transformation kinetic model could be properly used.

For the simulation, a cylindrical 1045 steel specimen was used with a length of 101.6 mm and a diameter of 25.4 mm. The total number of nodes and elements were 306 and 250, respectively. The initial temperature was 845 °C and the bottom surface was quenched by spraying water, with natural air cooling on the side surfaces. Fig. 6 shows the elemental mesh that was used for the simulations.

5. Experimental verification

In order to verify the simulation results and to use the results to predict mechanical properties, two sets of experiments were performed: (1) end-quench tests on a 1045 steel and (2) isothermal heat treatments to produce various microstructures followed by hardness tests. Table 5 gives the chemical composition of the 1045 steel used in these experiments.

5.1. End-quench tests

End-quench hardenability tests, or Jominy tests, were conducted with the 1045 steel in accordance with ASTM A 255-07 [35]. Three samples were tested. The sample was 25.4 mm in diameter and 101.6 mm in length. An austenitization treatment in a box furnace at 845 °C for 1800 s was performed prior to quenching. Hardness traverses (Rockwell C scale) were conducted along the length of the sample to obtain the standard hardenability curve. Photomicrographs were taken along the length of the sample. Quantitative values for the microstructural constituents were determined by image analysis.

Table 5
Chemical composition (weight percent) of 1045 bar steel.

C	Mn	Si	Cu	Ni	Cr	Mo	V	N
0.45	0.80	0.24	0.39	0.10	0.16	0.024	0.028	0.008

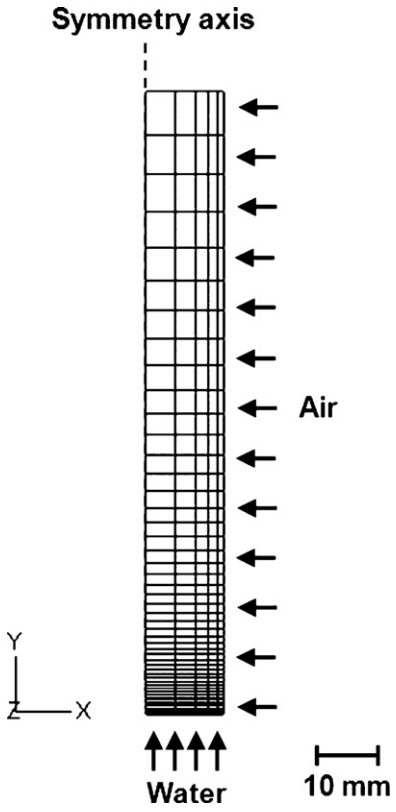

Fig. 6. Finite element mesh used to simulate the end-quench experiments.

5.2. Isothermal heat treatments

For hardness predictions after end-quenching standard hardness values for the 1045 steel were needed for each of the constituent microstructures. The experimental isothermal heat treatments temperatures used to produce the various microstructural constituents were obtained from the IT diagram. Disk specimens 25.4 mm diameter and 6.2 mm thick were austenitized at 845 °C for 600 s. A holding time of 3600 s at 600 and 400 °C in a salt bath was used to produce the ferrite/pearlite and the bainite microstructures, respectively. The martensite phase was obtained by direct water quenching. The hardness (Rockwell C scale) of heat-treated samples was measured. Table 6 gives the average hardness values for the three different microstructures of the 1045 steel.

6. Results

Fig. 7 shows the temperature variation with time for the bottom surface of the end-quenched sample and the temperature located along the center line of the sample at a distance 101.6 mm from the quenched end. Fig. 7 also shows the convective heat-transfer coefficient for the water-quenched end of the sample as a function of the surface temperature [36]. These calculated values appear to be quite reasonable, and provide confidence in the thermal aspects of the simulation work.

Figs. 8 and 9 show the results of the kinetics model. In Fig. 8, the volume fraction of the microstructural constituents in the bottom 25 mm of the end-quenched sample are given. As expected, the region nearest the water-quenched end is essentially all martensite, with bainite becoming the dominant constituent in deeper regions where the cooling rate is lower. Ferrite begins to appear about 15–20 mm from the quenched end as the amount of bainite begins to diminish. Pearlite begins to form in the sample at depths

Table 6
Average hardness values (HRC) for the various microstructures in 1045 steel.

Ferrite/pealite	Bainite	Martensite
17.8	26.8	58.1

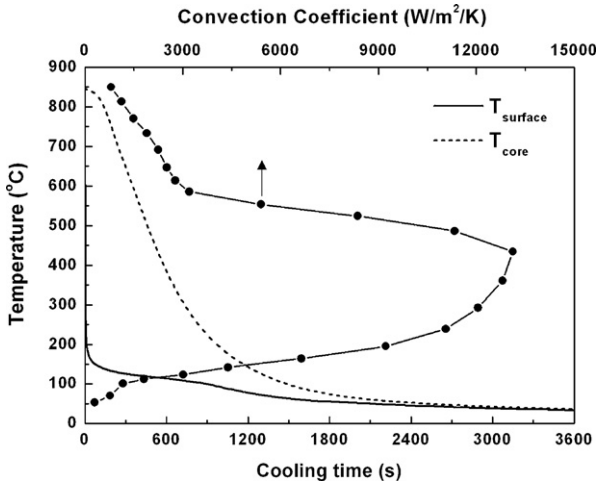

Fig. 7. The temperatures at surface and center locations for the end-quench simulation. The convective heat-transfer coefficient as a function of surface temperature is also shown.

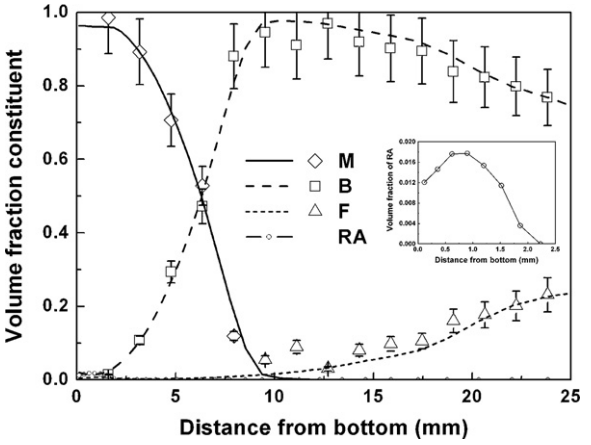

Fig. 8. Volume fraction of the various microconstituents as predicted from the end-quench simulation. Data points are for experimentally values obtained by image analysis. Insert shows the amount of retained austenite (RA) as a function of distance in the region close to the quenched end.

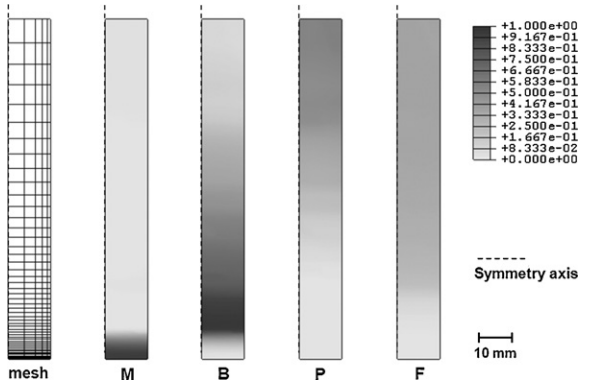

Fig. 9. Distribution of various microconstituents in the end-quenched sample as predicted by the simulation (M: martensite, B: bainite, P: pearlite and F: ferrite).

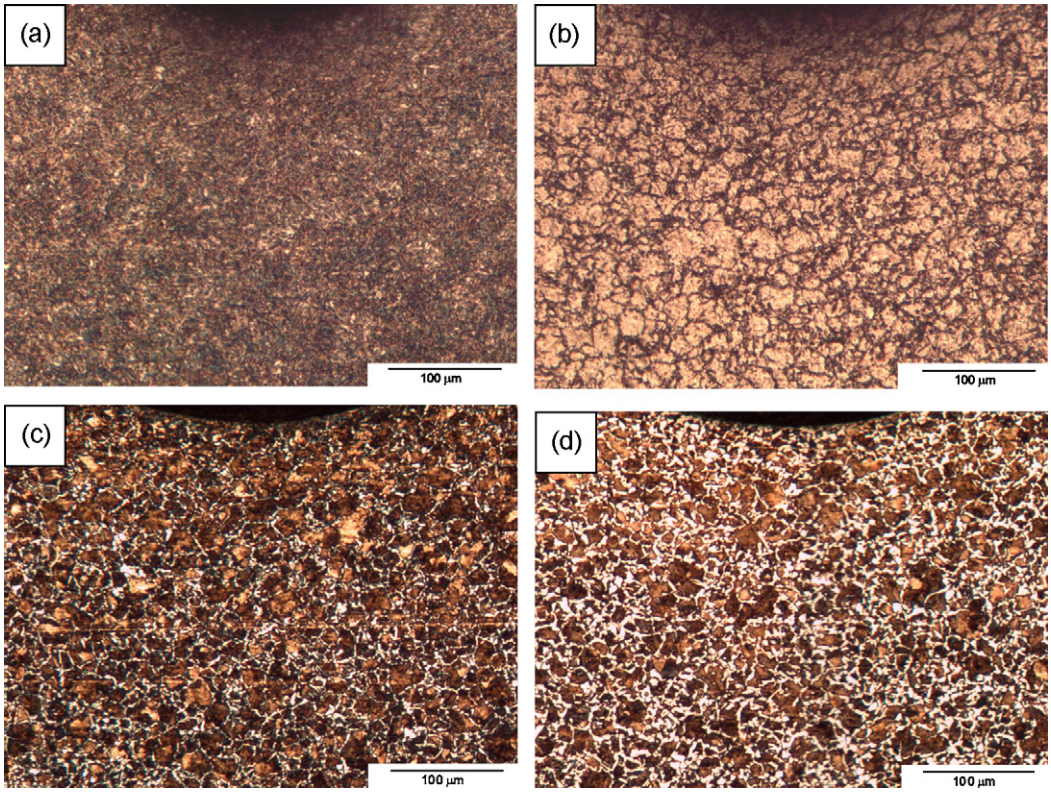

Fig. 10. Microstructures from various locations in the experimental specimen. (a) 1.6 mm from quenched end, (b) 4.8 mm from quenched end, (c) 11.2 mm from quenched end, (d) 23.9 mm from quenched end. The hardness indentation is shown at the top of each photomicrograph to aid in determining the specific location.

greater than 25 mm, as shown in Fig. 9. Fig. 8 gives the experimentally measured volume fractions for the different constituents. There is very good agreement with the model predictions and the experimental data.

Based on Figs. 8 and 9, at the quenched end of the specimen where the cooling rate is the highest, martensite is predicted to be the dominant microconstituent, with only a maximum of 3% retained austenite predicted. The cooling rate decreases as the distance from the quenched end increases. With the decrease in cooling rate, the austenite decomposes to other products instead of martensite. Bainite is the first new product to form, replacing martensite, and reaches a maximum volume fraction at a distance of approximately 10 mm from the quenched end. The maximum depth of martensite transformation is predicted at 10 mm, which corresponds with the maximum bainite volume fraction. At distances greater than 10 mm, the bainite volume fraction decreases as the austenite transforms to ferrite and eventually pearlite.

Fig. 10 shows photomicrographs from the end-quenched sample. In each photomicrograph the indentation due to the hardness test is captured. Having the hardness indentation allowed a more accurate determination of the distance from the quenched end. Fig. 10(a) shows the microstructure 1.6 mm from the quenched end, which is essentially all martensite. Fig. 10(b) is located at 4.8 mm and shows a mixture of mostly martensite with some bainite. The microstructure in Fig. 10(c) is 11.2 mm from the quenched end and contains bainite with some ferrite. Fig. 10(d) is located 23.9 mm from the quenched end and consists of bainite with even more ferrite than Fig. 10(c). These photomicrographs provide qualitative verification of the kinetics model with regard to the microstructures predicted.

Fig. 11 shows the hardness profile of the 1045 sample. These hardness points comprise the standard hardenability curve for the 1045 steel. Fig. 11 also shows the hardness values calculated from the simulation as a function of distance. The calculation was based upon the kinetics model prediction of constituent volume fraction and the hardness prediction based on the constituent volume fraction in the microstructure. Further details about this calculation are presented in Section 7. Overall, the prediction of hardness as a function of distance for the end-quenched sample matches the experimental data well.

7. Discussion

7.1. Comparison with previous kinetics models

The original transformation model by Kirkaldy and Venugopalan [2] was later modified by Li et al. [1]. Both models consist of two functions as shown in Eq. (1): the function, $g(V)$, is an integrated

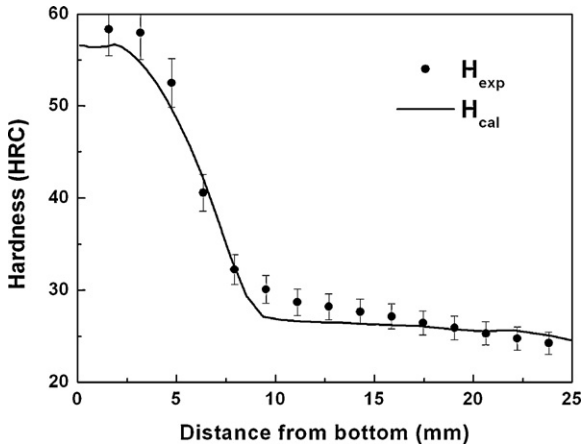

Fig. 11. Hardness profile from the end-quench simulation (solid line) compared to the experimentally measured hardness data.

function related to microconstituent volume fraction and the other function, $f(T)$, accounts for the effects of chemical composition and temperature dependence on the transformation. The integrated function is called the reaction rate, $R(V)$, and it determines the start and finish times of transformation and the kinetics rate during transformation. Even though the second function, $f(T)$, changes due to chemical composition and transformation temperature, the integrated function applies for all transformations, independent of composition or transformation temperature. The integrated forms proposed by Kirkaldy (R_K) and Li (R_L) were optimized using experimental phase-transformation diagrams to obtain:

$$R_K(V) = \int_0^V \frac{dV}{V^{2(1-V)/3}(1-V)^{2V/3}} \tag{9}$$

$$R_L(V) = \int_0^V \frac{dV}{V^{0.4(1-V)}(1-V)^{0.4V}} \tag{10}$$

The model in the present study used a different integrated function, as shown in Eq. (6), which was obtained by modification of Li's integrated function. A linear volume fraction term was added for each phase transformation in the present model. These additional terms predict the phase-transformation kinetics more accurately, as shown by the predicted IT diagram in Fig. 5. The equivalent integrated function for the present model is:

$$R(V) = \int_0^V \frac{(a - b \cdot V)dV}{V^{0.4(1-V)}(1-V)^{0.4V}} \tag{11}$$

where the values of a and b depend on the specific diffusional transformation.

The ratio of the incubation time (τ) for 1% volume fraction to that for 0.1% volume fraction was reported to be about 4 by the experimental observation of Kirkaldy and Venugopalan [2]. However, Eq. (9) (i.e. Kirkaldy's function), indicates that this ratio is about 2.14. This discrepancy was mentioned by Li et al. [1], and Li's function (i.e. Eq. (10) was successfully modified to predict the experimentally observed ratio of approximately 3.95). From Eqs. (4)–(6), the same ratio ($\tau_{1\%}/\tau_{0.1\%}$) was calculated to be between 3.93 and 3.95 for the three different diffusional transformations.

The transformation reaction time ($\tau_{100\%}/\tau_{1\%}$), which is the same as $R(1)/R(0.01)$, was compared from Kirkaldy's model and Li's model. The reaction time of 6.8 calculated from Kirkaldy's model is approximately three times faster than that the value of 19.7 obtained by Li's model. Li showed that the difference between these two reaction times predicted by Kirkaldy's and Li's models yields quite different hardness predictions for a 4140 steel, even though IT diagrams predicted by both models compare favorably with the experimental IT diagram. Li attributed the difference in hardness especially for medium- and high-alloyed steels to the faster reaction rate in Kirkaldy's model. Ironically, the reaction function contains no term to account for the effects of alloying elements. It seems reasonable to use a different reaction rate function, depending on the type of phase transformation or differences in steel chemical compositions. Thus, the usage of different reaction rate functions in this study should enable a more accurate model for the transformation kinetics for the 1045 steel. The range of the predicted reaction rates for the model in this study is 6.6–12.5.

7.2. The bainite transformation

For the bainite transformation, many studies have been presented to address its incompletion. In particular, Bhadeshia and Waugh [37] studied the incompletion of the bainite transformation. A supplemental term to express the sluggishness of the bainite transformation was used in Kirkaldy's model [2]. The supplemental term in the integrated function depends on chemical composition and volume fraction. The modified reaction function of the bainite transformation was similar to the basic form of the reaction rate in the present model. The addition of the supplemental term makes an asymmetric sigmoidal curve to express the sluggishness of bainite formation. The sigmoidal curves predicted by Eqs. (9) and (10) are symmetric below 50% volume fraction and above 50% volume fraction. Fig. 12 shows the comparison of the reaction rate expression obtained from Eqs. (9) and (10) and the reaction function from Eq. (11) for the bainite transformation. It is observed that relative integration value for Kirkaldy's model and Li's model equals 0.5 at a bainite volume fraction of 0.5. In contrast, the relative integration value is 0.68 at a bainite volume fraction of 0.5 for the model in the present study. Fig. 12 also shows that the reaction rate in Eq. (11) is asymmetrical indicating that as the volume fraction of bainite reaches 100%, the reaction slows down, which is indicative of the retarded kinetics of bainite as its transformation reaches completion. This result also indicates that the integrated function for the reaction rate was reasonably modified to incorporate some physical meaning in the present study.

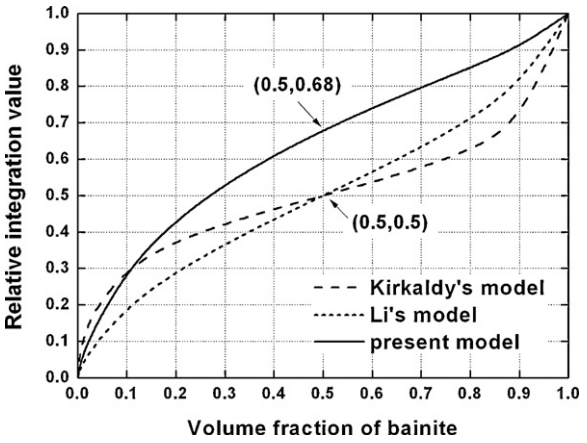

Fig. 12. Comparison of reaction rate functions for bainite transformation.

7.3. Chemical composition and temperature effects

The second function in the original Kirkaldy model contains parts related to alloying and temperature. Similar to the modification of Li's model from Kirkaldy's model, the temperature related part from Li's model was used without change in the present study. An activation energy term for transformation and undercooling below the equilibrium temperature are included in the temperature factor. The kinetics parameter related to alloying elements of the previous two models consisted of effects of chemical composition and prior austenite grain size, but only one optimized parameter was used in our study. Table 7 compares the optimized values in Eq. (5) with the values from the models of Kirkaldy and Li for the chemical composition of the 1045 steel used in the present study.

As the kinetics parameter increases, the transformation kinetics become faster. The bainite kinetics parameter in Kirkaldy's model is a relatively large value—over twenty times than that of the other models. This large kinetics parameter accelerates the bainitic kinet-

Table 7
Comparison of kinetic parameters for 1045 steels.

	$A_{ferrite}$	$A_{pearlite}$	$A_{bainite}$
Kirkaldy's model	0.1678	4.4693	11619.5
Li's model	0.0351	1.4263	587.625
Present model	0.2128	2.3810	212.766

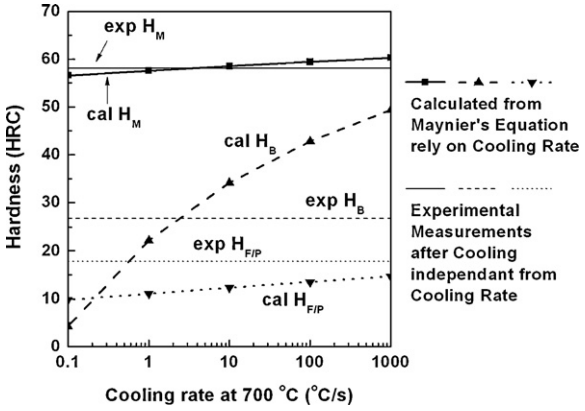

Fig. 13. Comparison of predicted and measured hardness values of each transformed phase according to cooling rate at 700 °C. The 'cal H_i' indicates the predicted hardness while the 'exp H_i' measured hardness. Subscript (i) indicates microconstituent (M: martensite, B: bainite, F/P: ferrite and pearlite).

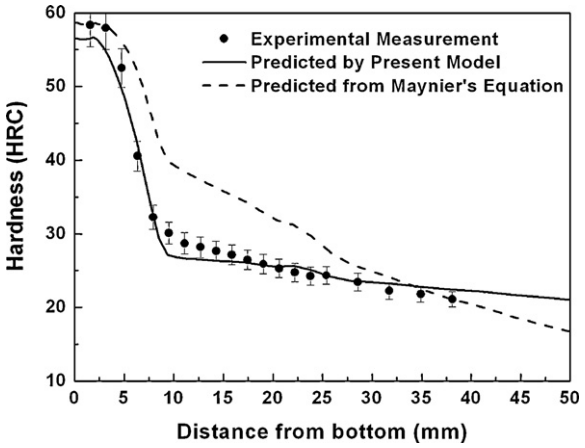

Fig. 14. Effect of accuracy of predicted and measured hardness data on final hardness in the end-quenched sample. Solid line: the calculated hardness using the measured hardness input data. Dashed line: the calculated hardness using the predicted hardness values from published equation.

ics, thus the additional term was required to express the retardation of bainite transformation. There is no consideration of manganese and silicon effects on the kinetics parameter in Kirkaldy's model except for the effect of manganese on the ferrite transformation. A nominal amount of silicon (0.25 wt.%) for the bainite transformation was assumed in Li's model but the silicon content affects the bainite kinetics even at low alloying levels [38]. In the present study a 1045 steel with higher residual copper was used. Copper could have an effect on transformation kinetics [39]. The neglect of copper and silicon causes the different kinetic parameters observed between three models as shown in Table 7.

7.4. Hardness values

From Fig. 8, it is seen that the maximum depth for any martensite in the steel is 10 mm from the quenched end. The hardness value sharply decreases from the quenched end at the depth of 10 mm. This result correlates with the variation of martensite volume fraction. As shown in Table 6, the measured hardness value of martensite is over two times larger than that of bainite and these measured values are quite reasonable. The empirical hardness equation proposed by Maynier et al. [40] has been used in many papers including those of Kirkaldy and Venugopalan [2] and Li et al. [1]. This empirical equation depends on chemical composition of the steel and cooling rate at 700 °C. Using the 1045 steel composition and cooling rate obtained from present simulations, the bainite hardness calculated by Maynier's hardness equation shows a large range from 22 HRC to 49 HRC. The calculated maximum bainite hardness is closer to the martensite hardness near the quenched surface (≈1 mm) where the cooling rate is greater than 950 °C/s.

Fig. 13 shows the change of calculated hardness according to chemical composition and cooling rate based on Maynier's equation compared with the measured hardness values, as shown in Table 6. For mixed microstructures a simple rule of mixtures was used to determine the overall hardness. The predicted hardness of martensite is very similar to the experimental hardness value, regardless of cooling rate. The predicted hardness of ferrite + pearlite shows reasonable agreement with the measured value especially at the higher cooling rates. In the case of bainite, however, the predicted hardness value is highly dependent on cooling rate. This variation in predicted bainite hardness results in an inaccurate hardness prediction of the end-quench simulation.

Fig. 14 shows the results of the end-quench simulation using the predicted hardness values from Maynier's equation overlapped on the results shown in Fig. 11. Maynier's equation predicts a higher hardness until the depth reaches ~35 mm because of the high hardness predicted for the bainite microconstituent. At depths over 40 mm, the hardness predicted by the simulation using Maynier's equation decreases gradually due to usage of lower hardness values of ferrite + pearlite than experimentally measured. This analysis provides evidence of the accuracy of the present study. Reliable experiment data were needed in order to determine the mechanical properties in the FEM simulation in the present study.

7.5. Specimen shape

The shape of the end-quench test specimen is not complicated; thus, there is no problem to treat the simulation as a one-dimensional heat-transfer analysis. However, the simulation used in the present approach using FEM analysis, coupled with phase-transformation models, can be expanded to more complex shapes in more than one dimension and with multiple heat treating steps. The temperature distribution during cooling is quite variable for different positions in a complex shaped sample.

8. Conclusions

The austenite decomposition kinetics for a 1045 steel was modeled using a set of equations that were a modification of the transformation model proposed by Li. The end-quench test was used to assess the model since it provides an experimental means of developing a variety of microstructures and a hardness profile. The prediction of microstructure by the kinetics model for the end-quenched sample was verified by examination of the microstructures observed in the end-quench experiment. The predicted hardness profile for the kinetics model was in good agreement with the experimentally measured hardness profile. The following conclusions have been reached:

- The kinetics model developed in the present study was compared to the kinetics models proposed by Kirkaldy and Venugopalan [2] and by Li et al. [1], which have been useful in predicting phase-transformation phenomena and to design heat treatment conditions for low alloy steels having a wide chemical composition range. The present model produces more accurate predictions, because it is a customized kinetics model based on the real measured kinetic data contained in the IT diagram.
- The hardness equation from Maynier [40] was evaluated, and for the 1045 steel investigated it predicted hardness values that were

greater than the experimentally measured values, especially for the bainite microstructure produced at fairly high cooling rates. By incorporating the hardness values from three simple experimental tests to obtain the hardness of martensite, bainite, and ferrite/pearlite in the 1045 steel, a more accurate hardness profile is predicted by the model. This result indicates that the material properties such as hardness values used in the simulation are very important and should be obtained if possible directly from experimental data.

- It is anticipated that the combination of kinetics model and material properties demonstrated in this work could be expanded/applied to other thermal/thermomechanical research fields where phase transformations occur and have a direct effect on mechanical properties, e.g. welding processes, TRIP (transformation induced plasticity) steel forming, phase-change random access memory device development, etc.

Acknowledgements

The support of the Advanced Steel Processing and Products Research Center at Colorado School of Mines is gratefully acknowledged.

References

[1] M.V. Li, D.V. Nieburh, L.L. Meekisho, D.G. Atteridge, Metall. Mater. Trans. B 29B (1998) 661–672.
[2] J.S. Kirkaldy, D. Venugopalan, in: A.R. Marder, J.I. Goldstein (Eds.), Phase Transformations in Ferrous Alloys, TMS-AIME, Warrendale, PA, 1984, pp. 125–148.
[3] W.A. Johnson, R.F. Mehl, Trans. AIME 135 (1939) 416–458.
[4] M. Avrami, J. Chem. Phys. 7 (1939) 1103–1109.
[5] A.N. Kolmorgorov, Izv. Akad. Nauk. SSSR. Ser. Matem (1937) 355–359.
[6] E. Scheil, Archiv f. Eisenhüttenw. 8 (1935) 565–567.
[7] M. Avrami, J. Chem. Phys. 8 (1940) 212–224.
[8] J.S. Kirkaldy, Metall. Trans. 4 (1973) 2327–2333.
[9] J.S. Kirkaldy, B.A. Thomson, E. Baganis, in: D.V. Doane, J.S. Kirkaldy (Eds.), Hardenability Concepts with Applications to Steel, AIME, Warrendale, 1978, pp. 82–125.
[10] M. Umemoto, N. Nishioka, I. Tamura, Trans. Iron Steel Inst. Jpn. 22 (1982) 629–636.
[11] P.K. Agarwal, J.K. Brimacombe, Metall. Trans. B 12B (1981) 121–133.
[12] M.B. Kuban, R. Jayaraman, E.B. Hawbolt, J.K. Brimacombe, Metall. Trans. A 17A (1986) 1493–1503.
[13] M. Suehiro, T. Senuma, H. Yada, K. Sato, ISIJ Int. 32 (1992) 433–439.
[14] J.L. Lee, H.K.D.H. Bhadeshia, Mater. Sci. Eng. A A171 (1993) 223–230.
[15] H.N. Han, J.K. Lee, H.J. Kim, Y.S. Jin, J. Mater. Proc. Technol. 128 (2002) 216–225.
[16] S. Serajzadeh, A.K. Taheri, Mater. Des. 25 (2004) 673–679.
[17] J.W. Christian, The Theory of Transformations in Metals and Alloys (Part I), 2nd ed., Pergamon Press, 1975, pp. 542–548.
[18] J. Cahn, Acta Metall. 4 (1956) 572–575.
[19] M. Lusk, H.J. Jou, Metall. Mater. Trans. A 28A (1997) 287–291.
[20] M.T. Todinov, Metall. Mater. Trans. B 29B (1998) 269–273.
[21] T. Réti, I. Felde, Comput. Mater. Sci. 15 (1999) 466–482.
[22] Y.T. Zhu, T.C. Lowe, Metall. Mater. Trans. B 31B (2000) 675–682.
[23] E.H. Bucknell, W. Steven, Progr. Metal. Phys. 1 (1949) 235–280.
[24] Thermo-Calc Software, http://www.thermocalc.se/.
[25] J. Miettinen, Metall. Mater. Trans. B 28B (1997) 281–297.
[26] T. Ericsson, S. Sjöström, M. Knuuttila, in: D.E. Diesburg (Ed.), Predicting Residual Stresses in Cases, Case Hardened Steels, Metallurgical Society of AIME, 1983.
[27] J.S. Kirkaldy, E.A. Baganis, Metall. Trans. A 9A (1978) 495–501.
[28] Y.K. Lee, M.T. Lusk, Metall. Mater. Trans. A 30A (1999) 2325–2330.
[29] Y.K. Lee, J. Mater. Sci. Lett. 21 (2002) 1253–1255.
[30] C. Capdevila, F.G. Caballero, C. García de Andrés, ISIJ Int. 42 (2002) 894–902.
[31] S.J. Lee, Y.K. Lee, ISIJ Int. 47 (2007) 769–771.
[32] American Society for Metals, Atlas of Isothermal Transformation and Cooling Transformation Diagrams, ASM International, Metals Park, OH, 1977.
[33] S.J. Lee, Y.K. Lee, Acta Mater. 56 (2008) 1482–1490;
Acta Mater 57 (2009) 2605.
[34] ABAQUS Version 6.5, Hibbitt, Karlsson & Sorensen, Inc., Rising Sun Mills, RI, 2005.
[35] American Society for Testing and Materials, Annual Book of ASTM Standards, vol. 1.03, ASTM International, West Conshocken, PA, 2007.
[36] K. Arimoto, T. Horino, F. Ikuta, C. Jin, S. Tamura, Explanation of the Origin of Distortion and Stress Distribution Patterns in Water-Quenched Chromium Steel Cylinders Using Computer Simulation, ASM Heat Treating Society Conference, Pittsburgh, PA, 2005, pp. 253–262.
[37] H.K.D.H. Bhadeshia, A.R. Waugh, Acta Metall. 30 (1982) 775–784.
[38] D. Quidort, Y. Bréchet, Scr. Mater. 47 (2002) 151–156.
[39] J.J. Wits, T.A. Kop, Y. van Leeuwen, J. Seitsma, S. van Der Zwaag, Mater. Sci. Eng. A A283 (2000) 234–241.
[40] P. Maynier, J. Dollet, P. Bastien, in: D.V. Doane, J.S. Kirkaldy (Eds.), Hardenability Concepts with Applications to Steel, AIME, Warrendale, 1978, pp. 163–176.